Frictional properties of shale reservoir rocks

Arjun H. Kohli[1] and Mark D. Zoback[1]

[1] We performed laboratory friction experiments on shale samples from three hydrocarbon reservoirs to assess compositional controls on fault slip behavior accompanying hydraulic stimulation. The samples span a range of clay and total organic content from ~10 to 60% by weight and demonstrate fine-scale heterogeneity within each reservoir. Friction measurements demonstrate strong dependence of strength and rate-state constitutive properties on shale composition. Shale samples with clay and organic content above ~30% by weight show coefficient of friction ~0.4 and consistently velocity-strengthening behavior, while those below this threshold show increased strength and velocity-weakening behavior. This transition in frictional strength and stability suggests a change in the shale grain packing framework from rigid clast supported to clay mineral and organic matter supported. Measurements of gouge dilatancy further support these relationships, showing a negative correlation with clay and organic content. Critical slip evolution distance exhibits similar dependence on composition, implying common micromechanical mechanisms for the observed transition in frictional behavior. We performed microstructural characterization of the experimental samples and observe changes in the gouge load-bearing framework and shear localization features consistent with these mechanical data. While these results can be applied generally to infer slip stability on faults in clay-bearing sedimentary rock, we employ the experimental data to place constraints on microearthquake magnitudes and the occurrence of slow shear slip on preexisting faults during hydraulic stimulation in shale reservoirs.

1. Introduction

[2] Fault frictional strength and stability depend on a range of coupled parameters, including mineralogy, hydraulic properties, fault morphology, and the state of stress. In this study, we focus on the effects of mineralogic composition and microstructural texture on the frictional properties of organic-rich shale reservoir rocks. In recent years, ~150,000 horizontal wells have been drilled and hydraulically fractured in North America alone in these settings. Approximately one third of the natural gas consumed in the U.S. and an increasing amount of liquid hydrocarbons are produced from organic-rich shale formations. Due to their increasing production levels and extensive estimated reserves, these formations have been identified as a critical resource in facilitating the transition to less carbon intensive energy economies [*Flavin and Kitasei*, 2010; *Zoback et al.*, 2010; *Cathles*, 2012].

[3] Despite the importance of these resources, and the thousands of hydraulic fracturing operations carried out in organic-rich shales every day, the deformation mechanisms that accompany multistage hydraulic fracturing in these settings remain poorly understood. Because of their inherent low permeability, production from these reservoirs requires inducing slip on naturally occurring faults and fractures through fluid pressurization at the minimum principal stress. This process lowers the effective normal stress on potential slip surfaces, inducing microseismic events on critically stressed faults that are oriented for slip in given the stress field [*Zoback*, 2007]. The resultant microseismic events cluster around the hydraulic fracturing stages, enhancing formation permeability through shear slip and resultant inelastic damage in the surrounding rock. The event locations are classically assumed to define the volume of the reservoir in which stimulation occurs and from which gas is produced [*Warpinski et al.*, 2012]. Although this paradigm is widely used in well completion strategies every day, it has been shown recently that the number of events in each hydraulic fracturing stage does not correlate with the observed production [*Moos et al.*, 2011; *Vermylen and Zoback*, 2011; *Zoback et al.*, 2012]. In addition, mass balance analysis of microseismic deformation shows that the cumulative shear slip and damage can only account for a small fraction of the volumetric deformation implied by production [*Warpinski et al.*, 2012; *Zoback et al.*, 2012; I. Das and M. D. Zoback, Long period, long duration seismic events during hydraulic stimulation of shale and tight gas reservoirs part 2: Location and mechanisms, submitted to *Geophysics*, 2013b].

[4] These observations strongly suggest that in addition to the microseismic events, other deformation mechanisms are

---

[1]Department of Geophysics, Stanford University, Stanford, California, USA.

Corresponding author: A. H. Kohli, Department of Geophysics, Stanford University, 397 Panama Mall, Stanford, CA 94305, USA. (ahkohli@stanford.edu)

Table 1. Shale Sample Composition From the Three Reservoir Study Areas

	Depth (m)	Illite	Illite/Smectite	TOC	Clay + TOC	Quartz	Calcite	Pyrite	Other
Barnett									
1	2608.76	5.40	0.60	3.20	9.20	58.70	19.80	2.10	10.20
2	2615.73	21.30	9.20	4.30	34.80	42.10	21.30	1.30	0.50
3	2634.20	20.80	13.60	5.70	40.10	52.40	0.30	1.80	5.40
4	2633.70	23.60	13.80	5.30	42.70	51.30	0.00	1.70	4.30
Haynesville									
1	3481.42	23.00	1.00	1.82	25.82	16.00	52.00	2.00	4.18
2	3439.20	31.72	12.00	3.08	46.80	25.00	21.00	2.00	5.20
3	3439.20	43.50	5.89	2.84	52.23	20.00	25.20	2.40	0.10
Eagleford									
1	3864.39	10.30	2.04	1.86	14.20	13.10	69.40	3.20	0.10
2	3862.75	14.30	13.40	2.10	29.80	8.40	60.50	0.85	0.45

active in these unconventional reservoirs during hydraulic fracturing and contribute significantly to production. In recent analysis of microseismicity from the Barnett shale, Texas, *Das and Zoback* [2011] report on relatively long-period, long-duration (LPLD) slip events occurring during hydraulic fracturing, which strongly resemble the form of tectonic tremor recorded in plate boundary fault zones [*Obara*, 2002; *Shelly et al.*, 2007; *Peng and Gomberg*, 2010]. As abundant evidence indicates that tectonic tremor is caused by subseismic slip on faults at depth [*Beroza and Ide*, 2009], *Das and Zoback* [2011, submitted manuscript, 2013b] and *Zoback et al.* [2012] hypothesize that the LPLD events observed in the shale reservoirs are also caused by slow shear slip on large preexisting faults. Present understanding of these processes and their relationship to production is limited, motivating further investigations of the fundamental mechanical properties governing slip stability in shale reservoirs.

[5] Previous laboratory friction studies of the effects of mineral composition have focused on clay-rich lithologies, which are abundant in mature fault zones [*Chester et al.*, 1987; *Underwood*, 2002; *Solum et al.*, 2006; *Schleicher et al.*, 2010; *Chester et al.*, 2012], as well as shale reservoirs [*Ross and Bustin*, 2009; *Passey et al.*, 2010], and are generally considered a first-order control on fault strength in the upper crust [*Bird*, 1984; *Vrolijk*, 1990; *Vrolijk and van der Pluijm*, 1999; *Deng and Underwood*, 2001; *Moore and Lockner*, 2007; *Ikari et al.*, 2007, 2009; *Tembe et al.*, 2010]. Early laboratory studies characterize the frictional strength of clay-rich fault gouges, demonstrating significant weakness relative to Byerlee's rule [*Byerlee*, 1978] and stable sliding at high confining pressures in samples with clay contents as low as ~15% [*Summers and Byerlee*, 1977; *Shimamoto and Logan*, 1981]. Although these relationships were suggested as early as *Skempton* [1964], the first systematic experimental study of the effects of clay content on frictional strength was conducted by *Lupini et al.* [1981], who described a three-regime model for the loss of strength with increasing clay content: (1) "turbulent shear" (<25 wt% clay) represented by a moderate decrease in strength, (2) "transitional" (<70 wt% clay) represented by a significant drop in strength, and (3) "sliding shear" (~100 wt% clay) represented by a minimum in strength. More recent studies vary clay mineralogy in order to study frictional behavior in response to changes in slip velocity, utilizing rate-state friction theory [*Dieterich*, 1979; *Ruina*, 1983] to quantify frictional stability and slip evolution behavior [*Marone et al.*, 1990; *Marone*, 1998; *Saffer et al.*, 2001; *Saffer and Marone*,

2003; *Ikari et al.*, 2007, 2009; *Tembe et al.*, 2010; *Moore and Lockner*, 2011]. *Saffer and Marone* [2003] attempt to correlate the conditions for transformation from "swelling" to "nonswelling" clays in the Earth with the transition from unstable to stable slip behavior; however, the combined effects of changing stress state, water content, and mineralogy with depth cannot be sufficiently explained by changes in frictional behavior between various clay types [*Ikari et al.*, 2007, 2009]. Other studies examine the controls of clay and phyllosilicate content on frictional behavior in binary and ternary synthetic mixtures and find that increasing the fraction of the more compliant phase results in lower frictional strength and produces relative slip stability [*Takahashi et al.*, 2007; *Moore and Lockner*, 2007; *Crawford et al.*, 2008; *Tembe et al.*, 2010; *Moore and Lockner*, 2011].

[6] Although many of these studies assess the frictional properties of clay-bearing gouges under a broad range of experimental conditions, no experiments have yet been conducted with actual material from specific areas of recorded slow slip or under conditions relevant to the deformation mechanisms occurring in shale reservoirs during hydraulic fracturing. In addition, most previous studies do not address some of the more complex phenomenon accompanying frictional slip such as slip evolution and dilatancy [e.g., *Marone and Kilgore*, 1993; *Samuelson et al.*, 2009], which can produce distinct frictional responses and include fault zone hydraulic properties in stability analyses [*Liu and Rubin*, 2010; *Segall et al.*, 2010]. During reservoir stimulation, the coupled interactions of frictional behavior, hydraulic properties, stress state, and fault characteristics determine frictional stability criteria. To begin to understand the physical mechanisms which produce distinct deformation behaviors during stimulation, we must first independently consider parameters that can be controlled at in situ conditions in the laboratory. Therefore, in this study we conduct friction experiments on dried natural samples from three shale gas reservoirs to primarily explore the effects of clay and organic matter content on frictional strength and stability. We employ rate-state friction theory to evaluate the results of these experiments in terms of friction rate dependence and slip evolution parameters. In addition, we perform microstructural investigations of the deformed samples to visualize the evolution in shale grain packing framework and shear localization features with composition. Based on these analyses, we assess the implications of compositional controls on shale frictional properties for the dynamics of fault slip during hydraulic stimulation.
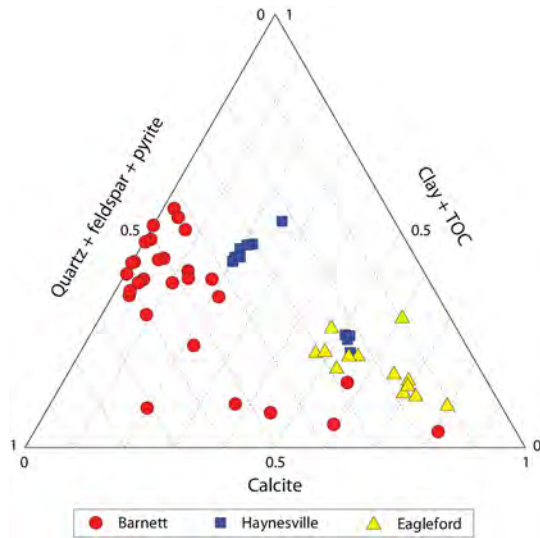
Figure 1. Shale sample composition from the three reservoir study areas in the ternary space of wt% QFP (quartz, feldspar, pyrite), clay and TOC (total organic content), and calcite.

2. Shale Samples

2.1. Composition

[7] Samples for this study are sourced from three shale gas reservoirs in Texas and Louisiana: the Barnett, Haynesville, and Eagleford shales. Cores were taken in both horizontal and vertical wells prior to hydraulic fracturing operations at various depths, stress states, and formation maturities. The Barnett reservoir samples were collected from a set of wells near the reservoir in which *Das and Zoback* [2011]

observed LPLD events during stimulation. Sample mineralogy (Table 1) was determined by powder X-ray diffraction (XRD) analysis and total organic content (TOC) was determined by thermochemical pyrolysis. Typical mineralogy in all reservoirs includes quartz, calcite, clay, dolomite, and feldspar. As each of these formations have gone through the smectite/illite transition [*Passey et al.*, 2010], the clay mineralogy is predominantly illite with accessory mixed layer illite-smectite, as well as <1 wt% kaolinite and chlorite in some samples. Other minor components include apatite, pyrite, and barite. Due to the complex mineralogy of these reservoirs, we choose to group clay and organic matter to study compositional controls on the mechanical behavior of these samples. H. Sone and M. D. Zoback (Mechanical properties of shale gas reservoir rocks part 1: Static and dynamic elastic properties and anisotropy, submitted to *Geophysics*, 2013a) studied a similar range of shale compositions from the same three reservoirs and found strong correlations between wt% clay and organic content and Young's modulus, motivating a simplifying classification of shale composition into the major compliant (clay, organic matter) and clastic (quartz, calcite, feldspar, pyrite) components. This classification proves convenient for analysis of the friction data because the dominant clastic components, quartz and calcite, have similar frictional strengths, ~0.7–0.8 [*Tembe et al.*, 2010; *Ikari*, 2010; *Ikari et al.*, 2011], enabling direct study of the effects of clay and organic content on shale grain packing framework and resultant mechanical properties. Furthermore, Sone and Zoback (submitted manuscript, 2013a; Mechanical properties of shale gas reservoir rocks part 2: Ductile creep, brittle strength, and their relation to the elastic modulus, submitted to *Geophysics*, 2013b) observed no discernible differences in elastic or creep
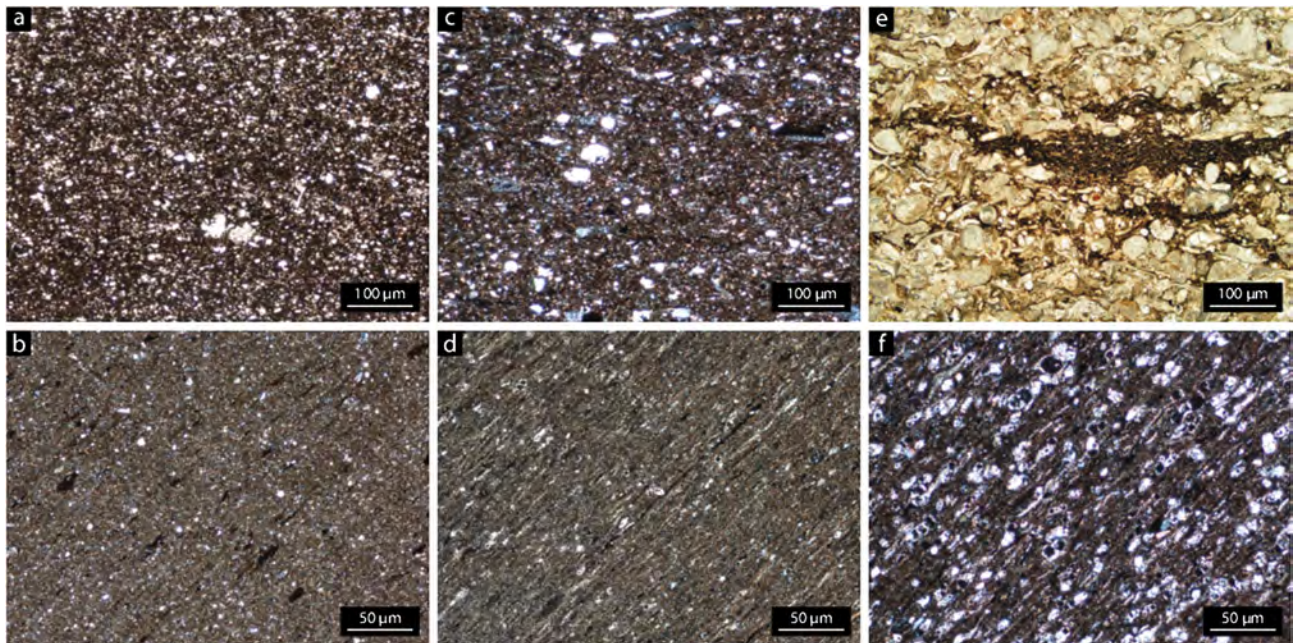

Figure 2. Photomicrographs (cross-polarized light) of intact starting material from the three reservoir study areas: (a) Barnett-1, (b) Barnett-3, (c) Haynesville-1, (d) Haynesville-2, (e) Eagleford-1, and (f) Eagleford-2. Sample bedding plane is oriented horizontally in the top row of images and at a 45° angle in the bottom row to highlight clay fabric development.
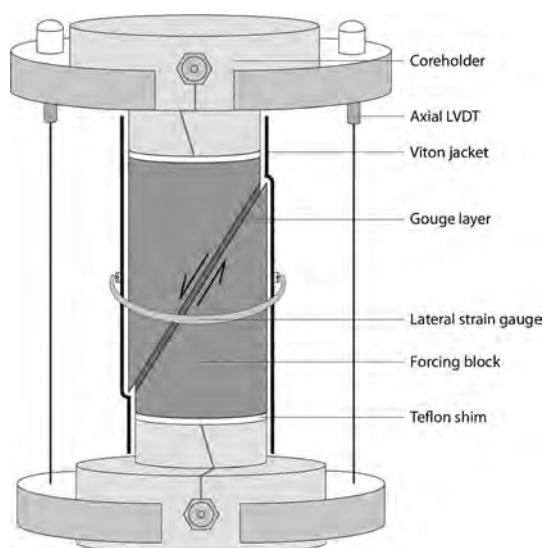
Figure 3. Friction experiment sample assembly inside triaxial pressure vessel.

properties at room dry conditions for siliceous and calcareous samples with similar clay and organic contents, reinforcing the utility of this classification for analysis of the dry shale framework. Shale samples span a range of clay and organic content from ~10 to 60 wt%, again representing both siliceous and calcareous lithologies, which reflects characteristic variations in each reservoir, but does not capture the full range of compositions present. Therefore, we find it most useful to illustrate the sample compositions for the three reservoirs in the ternary space of quartz, feldspar, pyrite (QFP), clay and TOC, and calcite (Figure 1).

2.2. Petrographic Observations

[8] Figure 2 shows petrographic images of several representative samples in the study from each reservoir. The general microstructure for all reservoirs is comprised of various proportions of fine-grained (<5 μm) illite clay matrix, lenses and/or thin veins (20–50 μm) of organic matter, biotic calcite grains (50–100 μm), and rounded to semiangular clasts (20–100 μm) of quartz, feldspar, and/or calcite. The top and bottom rows of images in Figure 2 depict relatively low and high clay and organic content samples for each reservoir, respectively; however, these samples do not represent absolute end-members in each reservoir. Fabric development is defined by preferred orientation of clay minerals, elongate lenses of organic matter of various aspect ratios, and detrital fossils, all of which delineate the sedimentary bedding plane. Sone and Zoback (submitted manuscript, 2013a) performed systematic petrographic characterization of similar shale samples and determined that the preferred orientation of the clay matrix, as defined by diagonal extinction positions in cross-polarized light, persists only in samples above ~30 wt% clay and organic matter. This is consistent with previous studies of preferred orientation of clay minerals as a function of decreasing silt content in shales [*Moon*, 1972; *Curtis*, 1980], and therefore, Sone and Zoback (submitted manuscript, 2013a, 2013b) interpret a transition in the load-bearing framework. For the purposes of this study, we are concerned primarily with the effects of clay and organic content on frictional strength and stability in the generalized lithologies of shale reservoirs. Therefore, we attempt to normalize microstructural characteristics of the intact samples that may result from differences in formation maturity [*Ahmadov*, 2011], burial history [*Moon*, 1972; *Revil et al.*, 2002; *Passey et al.*, 2010], and stress state, by crushing and reconstituting core material as gouge.

3. Experimental Procedures

3.1. Sample Preparation

[9] Friction experiments were conducted at room temperature and ambient humidity in a conventional triaxial configuration on 25.4 mm diameter cylindrical forcing blocks saw-cut at 30° to the core axis and filled with a ~2 mm thick layer of gouge (Figure 3). All shale samples were taken from 25.4 mm diameter cores, crushed completely, and passed over a 100# mesh sieve to obtain particle sizes <150 μm. The dry shale material was prepared as a paste with deionized water, spread onto the saw-cut face of the upper forcing block, and fit to form a cylindrical core with the lower forcing block. Both forcing blocks were composed of a porous reservoir sandstone. The assembly was then jacketed with 0.75 mm heat shrink Viton tubing and vacuum dried at 50°C for 5 h, after which it was sealed on steel coreholders on either side with wire tourniquets and loaded into the triaxial pressure vessel.

3.2. Triaxial Friction Procedure

[10] In the initial setup of each experiment, the samples were repeatedly cycled in confining pressure to 30 MPa, in order to allow the gouge layer to compact to a steady-state thickness and to remove any initial misalignments in the sample assembly. During this initial loading stage, the gouge layer thickness is observed to decrease by ~0.25–0.5 mm to an apparent steady state thickness, at which point no additional evolution occurs with application of cyclic loading steps. At the beginning of each test, an axial loading rate of 0.1 μm s^{-1} was applied until the sample reached initial peak shear stress. The sample was then subjected to a series of load point velocity steps 0.1–1.0–10 μm s^{-1} in constant displacement increments of ~0.25 mm along the sawcut. Each sample was tested at normal stresses of 10, 20, and 30 MPa, which were maintained by updating the confining pressure to account for the change in sliding contact area with slip along the sawcut. Confining pressure was controlled by the feedback signal from a pressure transducer with a precision of 0.05 MPa. During the experiments, axial load was measured by an internal load cell placed below the lower coreholder with a precision of 0.05 MPa and was corrected for the Viton jacket strength [i.e., *Tembe et al.*, 2010, Appendix A]. This results in an uncertainty of ~0.1 MPa in calculated shear and normal stresses, which manifests in an uncertainty of ~0.05 in the coefficient of sliding friction. Axial displacement was measured by a parallel set of linear variable differential transformers (LVDT) with a precision of ~1 μm and corrected for the elastic deformation of the steel coreholder and sandstone saw-cut assembly as a function of applied differential stress. The deformation of the sample perpendicular to the core axis was measured by a pair of spring-mounted strain gauges placed around the sample (Figure 3). By correcting for the saw-cut parallel slip and the change in

angle of the transducer with slip, evolution of the gouge layer thickness is recovered, assuming that all dilatant displacement occurs normal to the saw-cut plane. Slight thinning of the gouge layer with slip is observed in this experimental geometry and interpreted as extrusion of material on the saw-cut tips, analogous to the observations of gouge shear thinning in the double-direct shear experimental geometry [*Scott et al.*, 1994; *Samuelson et al.*, 2009]. Removing the shear thinning trend allows relative changes in gouge layer thickness of ~0.2 μm to be resolved at each velocity step. After the series of experiments at 30 MPa normal stress, the sheared sample assembly was impregnated with thin section epoxy and cut normal to the saw-cut surface in the direction of slip to produce thin sections of the gouge layer. Thin sections were prepared as single polished slides, in which the viewing side of the slide was carefully ground to expose the sample material. Microstructural observations were initially conducted via petrographic microscope, but because of the small particle sizes and prevalence of clay minerals in the gouge, the thin sections were mounted on aluminum sample posts and coated with gold for characterization via scanning electron microscopy (SEM) and energy dispersive spectroscopy (EDS).

3.3. Frictional Stability Measurement

[11] To evaluate the results of the velocity-stepping friction procedure, we apply the Dieterich-Ruina rate-state constitutive laws [*Dieterich*, 1979; *Ruina*, 1983], which have shown strong agreement with the results of laboratory friction studies of fault gouge [*Reinen and Weeks*, 1993; *Marone*, 1998; *Blanpied et al.*, 1998] and are widely applied to such velocity-stepping experiments [*Dieterich and Kilgore*, 1994; *Saffer and Marone*, 2003; *Samuelson et al.*, 2009; *Ikari et al.*, 2007, 2009, 2011; *Moore and Lockner*, 2011]. In this formulation, frictional stability is quantified by the steady state form of the constitutive relations through the friction rate parameter $(a - b)$:

$$(a - b) = \frac{\Delta f_{ss}}{\ln V/V_0} \quad (1)$$

in which Δf_{ss} is the change in the steady state coefficient of sliding friction in response to an instantaneous change in sliding velocity, from initial velocity V_0 to V; $(a - b) > 0$ indicates a rate-strengthening response, signifying that as sliding velocity increases, resistance to slip increases, thus promoting only stable sliding, while $(a - b) < 0$ indicates a rate-weakening response, signifying that as sliding velocity increases, resistance to slip decreases, allowing the potential for slip instability to nucleate [*Dieterich and Kilgore*, 1994; *Marone*, 1998]. These frictional responses represent steady state solutions of the single state variable form of the Dieterich-Ruina constitutive laws:

$$f(V, \theta) = f_0 + a\ln\left(\frac{V}{V_0}\right) + b\ln\left(\frac{V_0\theta}{d_c}\right) \quad (2)$$

$$\frac{d\theta}{dt} = -\frac{V_0\theta}{d_c}\ln\left(\frac{V_0\theta}{d_c}\right) \quad (3)$$

in which f_0 is the initial coefficient of friction, a and b are material parameters representing the change in friction in

response to a velocity step, and θ is a state variable, which evolves in time by equation (3), the slip law for state evolution [*Ruina*, 1983], one of several proposed state evolution laws. Frictional evolution in this formulation occurs over a critical slip displacement, d_c, which represents the slip required to reach a new frictional steady state or a new population of sliding contacts. At steady state, $\theta = d_c V_0^{-1}$ and is often interpreted as the average lifetime of sliding contacts. In this framework, d_c describes the distribution, or spacing, of load-bearing sliding contacts, or asperities. For complex natural materials such as shale, this entails contributions of grain size and shape, shape-preferred fabric, and mineralogy, which provides integrated micromechanical evidence of grain-scale deformation mechanisms.

[12] To relate friction measurements made in the laboratory to the model of rate-state friction, the finite stiffness of the specific apparatus must be accounted for to represent the elastic interactions of the gouge layer with the apparatus [*Marone et al.*, 1990]:

$$\frac{df}{dt} = K\left(V - V_{lp}\right) \quad (4)$$

in which K is the stiffness of the apparatus-forcing block system normalized by the applied normal stress on the axial face of the sample, and V_{lp} is the load point sliding velocity. We determined K for our experimental geometry by conducting constant normal stress loading on the sandstone forcing blocks without gouge and measuring the slope of the loading curve, $\Delta f \Delta d^{-1}$, until peak shear stress was reached [e.g., *Tembe et al.*, 2010]. To solve for constitutive parameters a, b, and d_c, we solve equations (3) and (4) for state variable and friction evolution, using equation (2) as constraint for friction rate dependence [e.g., *Saffer and Marone*, 2003]. This results in a nonlinear inverse problem, which can be solved using an iterative least squares method [e.g., *Reinen and Weeks*, 1993; *Blanpied et al.*, 1998], yielding best fit values of the rate-state constitutive parameters.

[13] In addition, for each applied velocity step, we measure the change in gouge layer thickness by removing the linear shear thinning trend from the calculated gouge layer thickness [e.g., *Scott et al.*, 1994; *Samuelson et al.*, 2009]. These effects have been readily quantified in many previous studies [*Marone and Kilgore*, 1993; *Ikari et al.*, 2009; *Samuelson et al.*, 2009] by the dilatancy parameter, α:

$$\alpha = \frac{\left(\frac{\Delta h}{h}\right)}{\ln V/V_0} \quad (5)$$

in which h is the instantaneous gouge layer thickness at the time of the velocity step and Δh represents the change in the gouge layer thickness, dilatancy (+) or compaction (−), in response to the velocity step.

4. Results

4.1. Frictional Strength

[14] Frictional strength as a function of slip displacement for samples from all three reservoirs is presented in Figure 4 for the series of experiments at 10 MPa normal stress. For each experiment, strength data are represented by the coefficient of
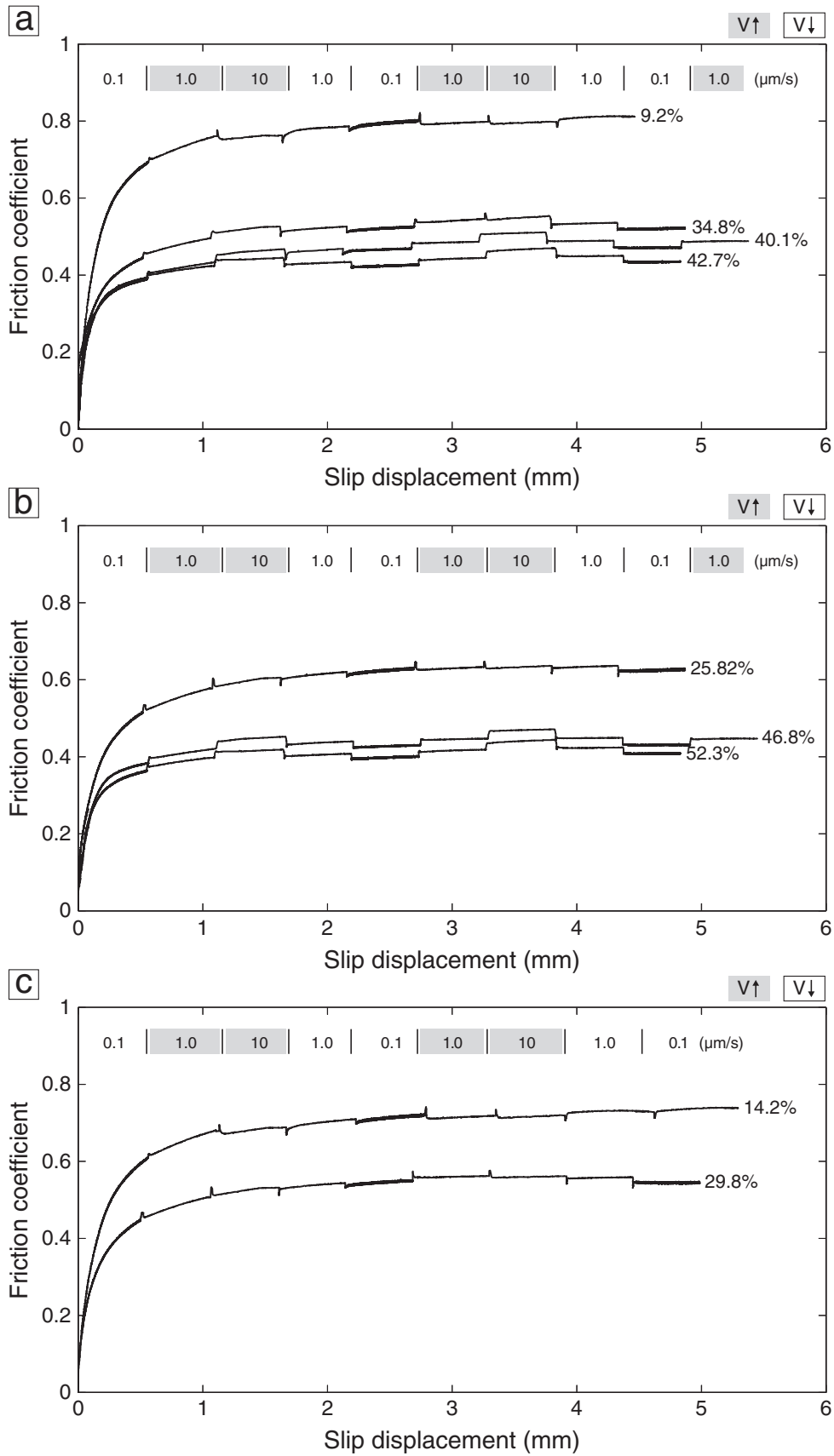
Figure 4. Friction-displacement curves for all samples at 10 MPa normal stress. Percentage labels show clay and organic content for each sample. Grey and white boxes denote imposed sliding velocity upsteps and downsteps, respectively. (a) Barnett shale. (b) Haynesville shale. (c) Eagleford shale.

Table 2. Friction Experiment Data Summary[a]

Sample	Clay + TOC (wt%)	Normal stress (MPa)	Friction coefficient	$(a - b)$	$(a - b)(-)$	$(a - b)(+)$	d_c (μm)	Δh (μm)
Barnett								
1	9.2	10	0.784	−0.0032	−0.0048	−0.0021	33.42	1.8
		20	0.79	−0.0023	−0.0044	−0.011	31.88	1.48
		30	0.778	−0.0030	−0.0041	−0.0015	33.12	1.28
2	34.8	10	0.511	0.0023	0.0006	0.0044	27.02	1.48
		20	0.521	0.0028	0.0008	0.0042	28.64	1.32
		30	0.514	0.0031	0.0011	0.0053	23.66	1.16
3	40.1	10	0.465	0.0049	0.0016	0.007	19.86	0.86
		20	0.4575	0.0057	0.0022	0.0074	20.26	0.78
		30	0.47	0.0053	0.0021	0.008	21.52	1.2
4	42.7	10	0.432	0.0062	0.0034	0.0094	20.36	1.06
		20	0.426	0.0070	0.0033	0.0085	15.36	0.68
		30	0.429	0.0068	0.0045	0.0089	10.52	0.74
Haynesville								
1	25.82	10	0.612	−0.0025	−0.0039	0.0003	20.74	1.16
		20	0.604	−0.0018	−0.0033	0.0005	15.14	0.68
		30	0.615	−0.0015	−0.0035	0.0007	21.4	1.22
2	46.8	10	0.427	0.0076	0.0052	0.0117	16.76	1.16
		20	0.433	0.0069	0.0042	0.011	14.22	0.72
		30	0.423	0.0079	0.0058	0.012	8.72	0.66
3	52.3	10	0.402	0.0084	0.005	0.0126	13.24	0.78
		20	0.399	0.0091	0.0044	0.0137	9.38	0.46
		30	0.404	0.0090	0.0066	0.0125	9.12	0.52
Eagleford								
1	14.2	10	0.698	−0.0029	−0.0044	−0.0009	31.66	1.84
		20	0.689	−0.0020	−0.0034	−0.0002	28.94	1.4
		30	0.701	−0.0034	−0.0048	−0.0015	29.76	1.5
2	29.8	10	0.567	−0.0018	−0.0035	0.0001	28.78	1.4
		20	0.575	−0.0017	−0.0033	0.0008	18.5	1.19
		30	0.563	−0.0013	−0.0027	0.0012	26.24	1.42

[a]Mineralogic constituents listed in weight percent (wt%). Friction coefficient is evaluated at 2 mm slip displacement along the sawcut. The parameters $(a - b)$, d_c, and Δh represent the average values for all velocity steps in a single experiment, and $(a - b)(-)$ and $(a - b)(+)$ represent the minimum and maximum values determined in a single experiment.

sliding friction, f, which is the ratio of the measured and corrected shear stress on the saw-cut plane, τ, to the applied effective normal stress on the saw-cut plane, σ_n:

$$f = \tau/\sigma_n \tag{6.1}$$

$$\tau = \frac{1}{2}(\sigma_a - P)\sin 2\Psi \tag{6.2}$$

$$\sigma_n = \frac{1}{2}[(\sigma_a + P) - (\sigma_a - P)\cos 2\Psi] \tag{6.3}$$

in which σ_a is the applied axial stress, P is the confining pressure, and Ψ is the angle between the core axis and the fault plane, in this case $\Psi = 30°$ [*Tembe et al.*, 2010].

[15] All experiments exhibit similar initial strengthening behavior, reaching a near-constant value of friction after shear strains of ~0.5, and strength is subsequently defined by a slight linear strain hardening trend. A summary of experimental parameters for all the tests in study is provided in Table 2. Frictional strength decreases monotonically as a function of clay and organic content within samples from each reservoir, as well as between samples from different reservoirs. Figure 5 depicts this relationship for all experiments in the study and shows that all frictional strengths are between ~0.4 and 0.8, which matches the approximate range of end-member strengths from the quartz-illite two-component system [*Crawford et al.*, 2008; *Tembe et al.*, 2010]. These studies on synthetic illite gouges also find a linear decrease in coefficient of friction with increasing clay content, generally consistent with the degradation of strength in shale samples with increasing clay and organic content; however,

although we can inform our results using the general descriptions of micromechanical evolution in these studies, we cannot strictly compare our results to those from studies of synthetic gouges, due to unknown effects of accessory mineralogy (Table 1) and surviving microstructure in shale reservoir rocks (Figure 2). Additionally, the measured friction strengths for the most clay-rich samples are also generally consistent with biaxial studies of natural, illite-dominated fault gouges [*Ikari et al.*, 2009; *den Hartog et al.*, 2012]; however, we again must temper comparisons to these data due to the difficulty in comparing natural microstructures. The cohesive, approximately linear trend in frictional strength as a function of clay
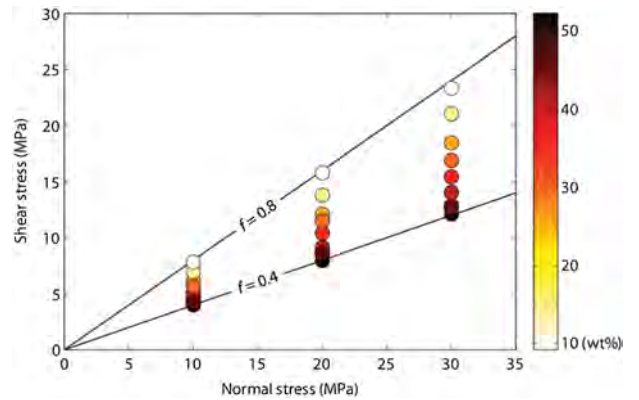

Figure 5. Measured shear stress at normal stresses of 10, 20, and 30 MPa for all samples in the study. Color bar shows clay and organic content for each sample.
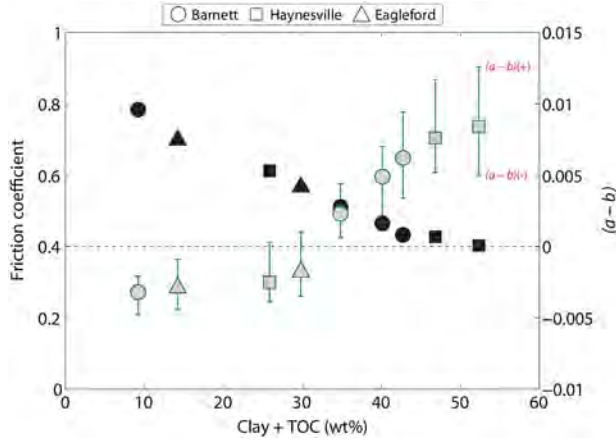
Figure 6. Friction coefficient (black symbols) and $(a - b)$ (grey symbols) as functions of clay and organic content at 10 MPa normal stress for all samples in the study. Values of $(a - b)$ are obtained from averaging the results of all velocity steps within a single experiment. Error bars represent the maximum, $(a - b)(+)$, and minimum, $(a - b)(-)$, values of $(a - b)$ observed in each experiment.

and organic content reflects the utility of the simplifying classification of shale composition, which normalizes variations in framework mineralogy and the relative proportions of clay and organic matter. Sone and Zoback (submitted manuscript, 2013a, 2013b) observe similar correlations of Young's modulus and viscoelastic creep with clay and organic content in experiments on dried core samples from the same shale reservoirs, reflecting the fundamental micromechanical controls on clastic and compliant component systems, even in the case where initial microstructure and in situ conditions are not normalized.

4.2. Friction Constitutive Properties

[16] For each velocity step in each experiment, we determine the best fit rate-state constitutive parameters a, b, and d_c, by the procedures described in section 4.3. Frictional stability or rate dependence is defined by the calculated parameter $(a - b)$, in which stable sliding is defined by $(a - b) > 0$ and potential instability is defined by $(a - b) < 0$. Figure 6 shows the variation of the coefficient of sliding friction and
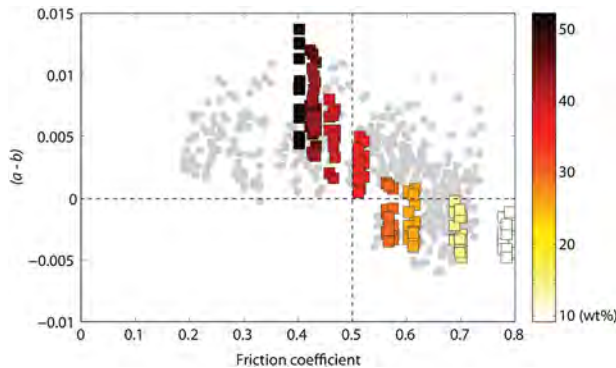
$(a - b)$ with clay and organic content for the series of experiments at 10 MPa normal stress from Figure 4. $(a - b)$ increases monotonically from -0.0048 to 0.0021 at the lowest clay and organic content until ~30 wt%, at which point a step transition to velocity strengthening behavior occurs, after which $(a - b)$ continues to increase, reaching a maximum value of $+0.005$ to 0.0126 at the highest clay and organic content. These values are consistent with broadly established constraints on frictional stability [*Ikari et al.*, 2011], which relate frictional strength and $(a - b)$ for a wide range of tested lithologies (Figure 7). At the highest clay and organic content, values of $(a - b)$ appear slightly greater than the scatter representing the large data set of friction experiments from *Ikari et al.*, while at lowest clay and organic content, values of frictional strength are greater than the range captured by *Ikari et al.*, but still support the same trend in $(a - b)$. Values of $(a - b)$ are also relatively insensitive to applied normal stress in the experiments and show no significant or systematic variation (Figure 8), consistent with double-direct shear experiments on illite shale gouge [*Ikari et al.*, 2009; *den Hartog et al.*, 2012]. *Tembe et al.* [2010] also observe increasing $(a - b)$ with increasing clay content in binary mixtures of illite and quartz, but do not record any transition from purely velocity-strengthening behavior.

4.3. Slip Evolution and Dilatancy

[17] In addition to evaluating frictional stability for each velocity step, we determined the rate-state frictional evolution parameter, d_c, and the dilatancy, Δh, by the procedures described in section 4.3. Figure 9 shows the variation of d_c with clay and organic content for all experiments in the study as functions of both shale composition and shear strain (color contours). Although d_c exhibits significant scatter for each value of clay and organic content, color contouring the points by the shear strain in gouge layer reveals d_c generally decreasing with increasing shear strain. However, this trend in d_c as a function of shear strain does not appear completely systematic, such that the decrease in d_c for a given increment of shear strain is nonunique. The scatter due to the shear strain dependence of d_c masks the dependence on clay and organic content, but, by determining the average value of d_c at each composition (grey circles), the negative correlation with clay and organic content appears stronger, although not monotonic.

Figure 7. $(a - b)$ as a function of coefficient of friction for this study (square symbols) and *Ikari et al.* [2011] (grey circles) adapted from *Ikari et al.* [2011]. Color bar shows wt% clay and organic content for each sample.
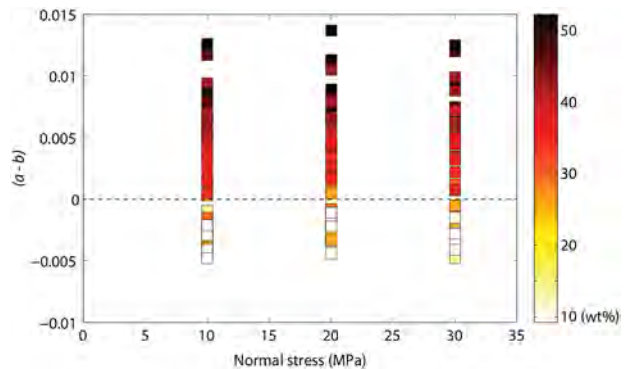

Figure 8. $(a - b)$ as a function of applied normal stress for all samples in the study. Color bar shows wt% clay and organic content for each sample.
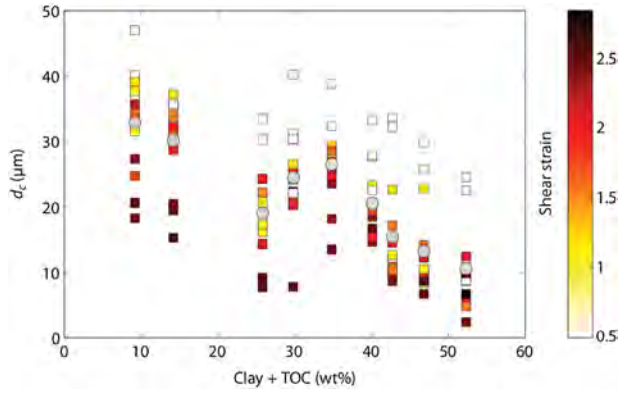
Figure 9. Critical slip displacement as a function of clay and organic content. Color bar shows shear strain in the gouge layer at the corresponding velocity step for which critical slip displacement was measured. Grey circles show average values of critical slip displacement for each composition.

Figure 11. Dilatancy as a function of clay and organic content. Color bar shows shear strain in the gouge layer at the corresponding velocity step for which dilatancy was measured. Grey circles show average values of critical slip displacement for each composition.

[18] Figure 10 shows a characteristic gouge layer dilation response for a sliding velocity upstep and downstep series. In this case, the lateral strain gauge measurement has been resolved as the normal to the plane of the sawcut and any shear thinning trend due to gouge extrusion at the saw-cut tips has been removed. In response to the change in sliding velocity from 1.0 to 10 μm s^{-1}, the gouge layer dilates ~2 μm from a normalized reference layer thickness and compacts ~1 μm in the subsequent downstep. The layer thickness evolution response correlates directly in time with frictional evolution and strongly resembles the results obtained by *Samuelson et al.* [2009] in double-direct shear experiments on simulated quartz gouge, as well as the form of dilatant evolution predicted by rate-state theory [*Segall and Rice*, 1995]. From these data, we determine the dilatancy, Δh, and the dilatancy parameter, α.

[19] Figure 11 shows the variation of Δh with clay and organic content for all experiments in the study. Plotting Δh in the same manner as d_c reveals remarkable similarities in their dependence on shale composition. In fact, values of Δh show similar scatter due to nonmonotonic dependence on shear

strain, with Δh also generally decreasing with increasing shear strain. Similar dependence of both parameters is also observed by *Marone and Kilgore* [1993] in double-direct shear experiments on quartz sand of varying grain size. The arithmetic mean of Δh (grey circles) imply a similar, nonmonotonic dependence on composition, with same the two samples between ~20 and 30 wt%, Haynesville-1 and Eagleford-2, deviating from a potential monotonic trend. The correspondence between these two parameters is represented in Figure 12 for each reservoir sample group and is unlikely coincidental, as they are measured by completely independent sensors in the friction experiments: d_c (internal load cell) and Δh (lateral strain gauge). Therefore, the deviation in slip evolution behavior of these intermediate clay and organic content samples from the compositional trend may be real, although not directly evidenced in the frictional strength or stability data. Separating the slip evolution data by reservoir (Figure 12) reveals similar monotonic and systematic trends for each sample group; however, while these data show similar slopes, they are apparently offset from one another in composition.

4.4. Experimental Gouge Microstructures

[20] We examined thin sections of the sheared gouge layers for the series of experiments at 30 MPa normal stress in a field emission gun SEM to evaluate micromechanical evidence for the observed friction behavior. To interpret mineralogy from microstructural morphology, we performed spot EDS measurements during SEM characterization, which allows for qualitative differentiation of mineral phases through X-ray measurements of atomic chemistry. Figure 13 shows secondary electron images of characteristic gouge microstructures for the range of clay and organic content spanned by the friction experiments. Figure 13a shows a typical mosaicked image of the sheared gouge layer for sample Haynesville-1, illustrating the development of shear localization features, which emerge at a low angle to the slip direction across the sample. These features are pervasively observed in gouge friction experiments [*Logan et al.*, 1992; *Tembe et al.*, 2010; *Ikari*, 2010] and are often attributed to the physical bounds of relatively rigid forcing blocks deforming gouge material [i.e., *Mandl and Luque*, 1977].
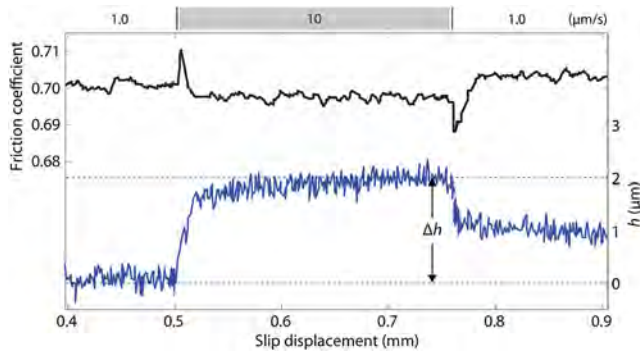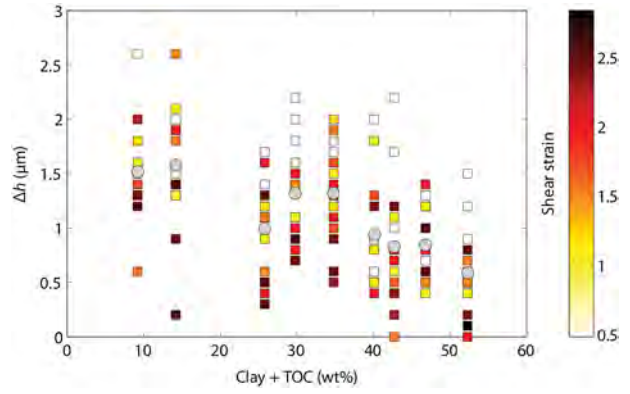

Figure 10. Example of gouge layer dilatancy measurement for sample Eagleford-2, after *Samuelson et al.* [2009]. (top) Detail of friction displacement curve for a velocity upstep and downstep sequence 1.0–10–1.0 μm s^{-1}. (bottom) Evolution of gouge layer thickness with slip displacement; dilatancy, Δh, is measured from a reference layer thickness from the previous velocity step (dashed lines).
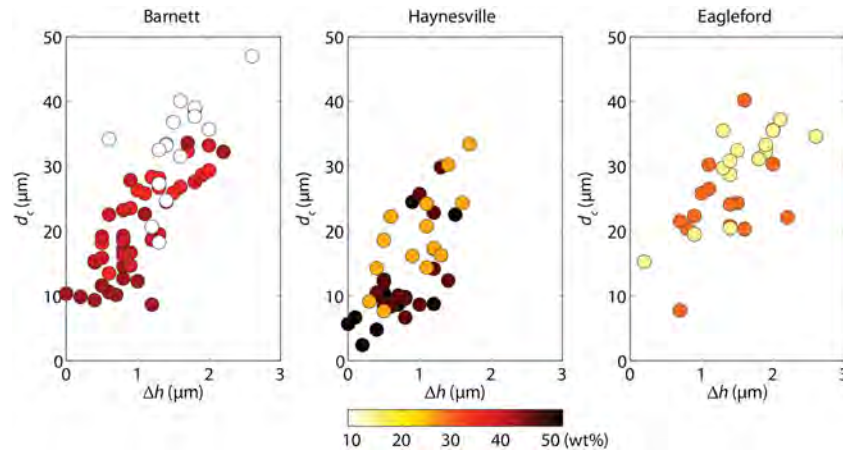
Figure 12. Correlation of critical slip displacement and dilatancy for each reservoir sample group, after *Marone and Kilgore* [1993]. Color bar shows wt% clay and organic content for each sample.

These features are dependent on shale composition, with low clay and organic content samples showing greater primary Riedel shear angle, R_1 (Figure 14), consistent with the detailed microstructural analyses of *Tembe et al.* [2010] on synthetic clay-quartz gouges. Furthermore, the compositional dependence of these macroscopic shear localization features is consistent with similar trends in d_c and Δh (Figures 9 and 11), which implies direct connections between bulk observations of frictional properties and microphysical slip evolution processes. Specifically, as clay and organic content increases, the slip-parallel (d_c) and slip-normal displacements (Δh) required to renew frictional steady state in response to a perturbation in slip velocity decrease, evidenced macroscopically by the reduction shear localization angle.

[21] Figures 13b–13j depict characteristic contact-scale microstructures in the experimental gouge samples and are ordered by increasing clay and organic content. Descriptions of the characteristic micromechanical features are provided in Table 3. Figure 13b illustrates clastic contact microstructure for sample Barnett-1, the lowest clay and organic content sample in the study. At this composition, only clastic contacts persist and pervasive grain-scale fracture is present, implying significant stresses are supported at these contacts, which is consistent with the observations of increased frictional strength. Figure 13c, Eagleford-1, reflects similar microphysical relationships, but, at this slightly lower clay and organic content, ~15%, clay fabric develops locally in isolated regions between clastic contacts (e.g., Figure 13d, Eagleford-1); however, adjacent grain-scale fractures and frictional strength consistent with Byerlee's rule suggest that these isolated concentrations of clay aggregates do not constitute the load-bearing framework at this composition. Figures 13e and 13f, Haynesville-1 and Eagleford-2, illustrate the further development of local clay fabric between clastic contacts near the observed compositional threshold for frictional stability. At ~30% clay and organic content, clastic contacts still predominate in the gouge framework, although a significant fraction of these contacts appear to be coated with clay particle aggregates and grain-scale fractures are not observed (e.g., Figure 13g; Eagleford-2). These aggregates form well-defined, slip-parallel fabrics in isolated regions of pure clay, but appear completely pinned in two

dimensions by clastic contacts, such that the fabric is locally disrupted around the clasts (e.g., Figures 13f and 13g; Eagleford-2) and is not continuous through the gouge layer. This signifies that although the proportion of clay contacts and the strength of local clay fabric increase, frictional strength and slip evolution are still controlled by the clastic components, which is consistent with observations of moderate frictional strength and negative to neutral friction rate dependence at this composition. Figures 13h–13j illustrate gouge microstructures for sample Haynesville-3, the greatest clay and organic content sample in the study. At this composition, the gouge microstructure is defined by a strongly developed, continuous clay fabric, which appears to host only isolated clasts, signifying the complete transition to clay and organic matter load-bearing framework. Additionally, within the clay fabric, relatively compacted domains form in regions of pure clay, which appear to function as framework supports in the gouge, while relatively dilated domains appear to form to due local fabric disruption from adjacent clasts (e.g., Figures 13i and 13j; Haynesville-3).

4.4.1. Role of Organic Matter

[22] Constraining the role of organic matter in frictional and microstructural properties of shale reservoir rocks remains challenging for several reasons. Since all samples in the study contain <10 wt% TOC and exhibit significant variations in clay content, ~10–40 wt%, it is not possible to isolate the effects of only organic matter content for these shale samples. Additionally, no existing studies constrain the frictional strength of the types of organic matter found in these shale reservoir rocks, requiring us to use microstructural and bulk mechanical analysis to constrain the role of organic matter. Figure 15 depicts characteristic organic matter microstructures in the experimental gouge samples and is ordered by increasing clay and organic content. Figure 15a, Barnett-1, depicts a narrow vein of organic matter pinned between populations of quartz grains in a clast-supported framework. At this composition, both clay and organic matter do not constitute the load-bearing framework, although both phases appear to coat clastic contacts, such that the morphology of clay aggregates and organic matter is dictated by the microstructural evolution of the local clastic contact population. Figure 15b, Haynesville-1, shows a consolidated lens of organic matter aligned in the local clay fabric, similar to the
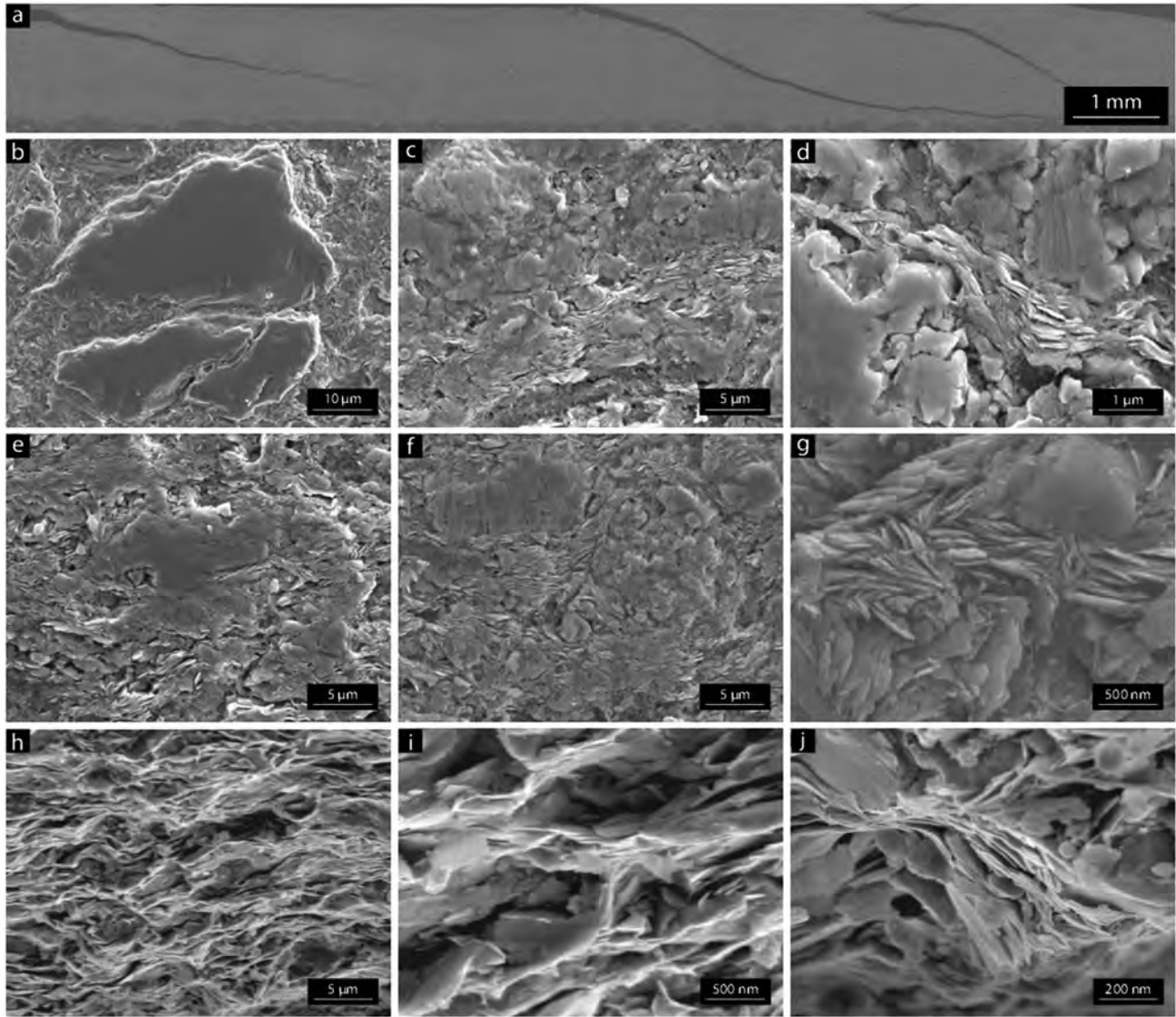
Figure 13. Secondary electron images of experimental gouge microstructures from test series at 30 MPa normal stress; sense of shear is top to the right in all images. Images are sequenced by increasing clay and organic content. (a) Haynesville-1, typical fault-normal thin section microstructure showing the development of typical shear localization features. (b) Barnett-1, at the lowest values of clay and organic content significant grain-scale fracture is observed. (c) Eagleford-1, at low values of clay and organic content local clay fabric develops, but never becomes spatially continuous. (d) Eagleford-1, although clay particles are present between some clastic contacts, grain-scale fracture still dominates. (e) Haynesville-1, at intermediate values of clay and organic content clay fabric development is still inhibited, but a greater proportion of clastic contacts are coated by clay particle aggregates. (f, g) Eagelford-2, at intermediate values of clay and organic content clastic barriers cause clay aggregates splay away from the shear plane inducing local fabric disruption. (h–j) Haynesville-3, at the highest values of clay and organic content clastic contacts are significant reduced and a strong clay fabric develops in the shear plane. Clasts become completely surrounded by clay aggregates and no grain scale fracture is observed. The sliding contact population is dominated by lens shaped clay aggregates aligned in the shear plane.

morphology of intact samples from the Eagleford reservoir (e.g., Figure 2f). In this case, the organic matter structure appears to have remained intact through the sample preparation process, possibly due to maturation-induced mechanical coupling with adjacent clay aggregates. Irrespective, organic matter lenses appear to function similarly to the isolated clay aggregates observed in samples below ~30 wt% clay and organic content (e.g., Figures 13c, 13e, and 13f) due to their coating of clastic contacts and alignment in the bulk shear direction. Above ~30 wt% clay and organic content, clay minerals appear to dominate the load-bearing framework (e.g., Figure 13h), such that the morphology of organic matter is dictated by the microstructural evolution of the local clay fabric. Figure 15c, Haynesville-2, illustrates elongate lenses of organic matter, which appear to be well aligned and elongated in the bulk shear direction, consistent with
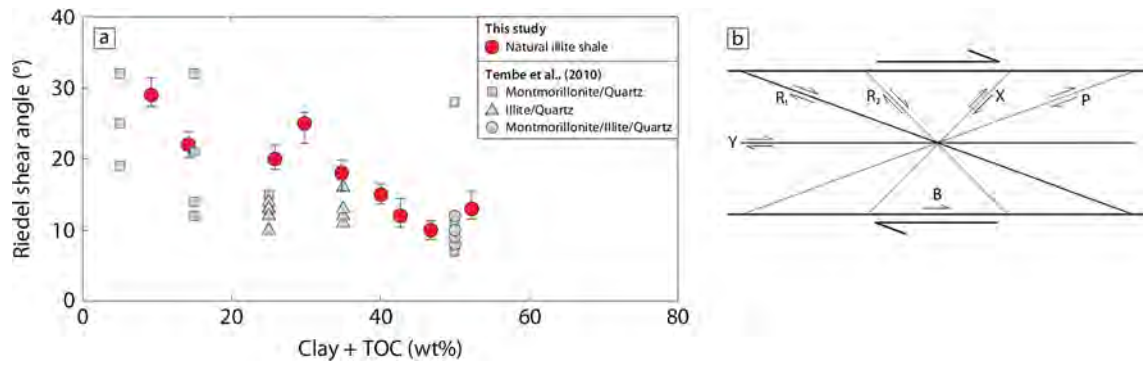
Figure 14. (a) Variation of Riedel shear angle, R_1, as a function of clay and organic content (red circles), after *Tembe et al.* [2010] (grey symbols). Error bars represent maximum and minimum values of measured shear angle for each thin section. (b) Schematic depiction of frequently observed shear localization features in fault gouge, after *Logan et al.* [1992].

measurements of slip evolution parameters and shear localization features at this composition. Although there does appear to be systematic relationships between clay and organic content and the angle of organic matter features to the bulk shear direction, we do not attempt to assess their significance in context of this study.

5. Discussion

5.1. Microphysical Model for Compositional Controls on Shale Friction

[23] The mechanical and microstructural observations of shale gouge friction appear to be generally consistent with a grain packing framework model, as developed by previous experimental studies on clay-bearing fault gouge [*Lupini et al.*, 1981; *Takahashi et al.*, 2007; *Crawford et al.*, 2008; *Tembe et al.*, 2010]. Lupini et al. present a three-regime model for the loss of frictional strength with increasing clay content, only two of which are relevant to the shale compositions studied here: (1) "turbulent shear" (<25 wt% clay) represented by a moderate decrease in strength, attributed to a transition to interconnected, load-bearing clay matrix, and (2) "transitional" (<70 wt% clay) represented by a significant drop in strength, attributed to Riedel shear localization and clay fabric development. Although shale reservoir rocks qualitatively evidence these transitions in gouge microstructure, frictional strength decreases by an approximately linear trend (Figure 6) and no abrupt drops in strength are observed with increasing clay and organic content. In addition, an abrupt transition in friction rate dependence occurs at ~30 wt% clay and organic content, consistent with petrographic (Figure 2) and elastic (Sone and Zoback, submitted manuscript,

2013a) evidence for the change in the shale load-bearing framework. Although this transition appears to be roughly consistent with the model of Lupini et al., no direct comparison can be made due to the confounding effects of accessory clastic mineralogy, organic matter, and surviving microstructure or digenetic cement. Additionally, *Tembe et al.* [2010] note that the three-regime model of Lupini et al. was constructed based on data at low normal stress (<1 MPa), at which grain crushing and comminution in clastic phases such as quartz and calcite do not occur, so it cannot describe the experiment conditions here or the in situ conditions of shale reservoirs. Tembe et al. attempt to adapt the model to the conditions of crustal fault zones and present a conceptual description of the microphysical processes dictating the reduction in frictional strength with increasing clay content, in which a load-bearing framework of sand transitions to a clay matrix-supporting framework [*Tembe et al.*, 2010, Figure 11]. While the features of this model are qualitatively similar to the observed microstructures shale gouge, we again cannot strictly compare the mechanical and microstructural features of our experiments to this analysis based on synthetic binary and ternary mixtures of clay and clastic components. In addition to the lack of end-member compositions in the cored shale samples, comparing Tembe et al.'s Figures 11a and 11b with Figures 13b–13d (Barnett-1) demonstrates that even at the lowest observed clay and organic content (<10 wt%), shale reservoir rocks retain a fine grained matrix of clay, organic matter and accessory clastic minerals (Table 1), in contrast to the relatively high-porosity, space-filling model of clay-poor microstructure presented by Tembe et al. Although at this shale composition, the matrix does not constitute the load-

Table 3. Guide to Shale Gouge Microstructures in Figure 13[a]

Sample	Clay + TOC (%)	R_1 (deg)	Clay mineral fabric	Grain-scale fracture	Organic matter microstructures	Loading bearing component
Barnett-1 (Figures 13b–13d)	9.2	29	No fabric	Pervasive at framework contacts	Fracture fill, narrow veins	Quartz and calcite clasts
Eagleford-2 (Figures 13e–13g)	29.8	25	Slip parallel, local, disturbed	Common at framework contacts	Slip parallel lenses, biotic grain deposits	Clay-clast aggregates
Haynesville-3 (Figures 13h–13j)	52.3	13	Slip parallel, strong, pervasive	No fracture, few clastic contacts	Slip parallel lenses	Clay matrix

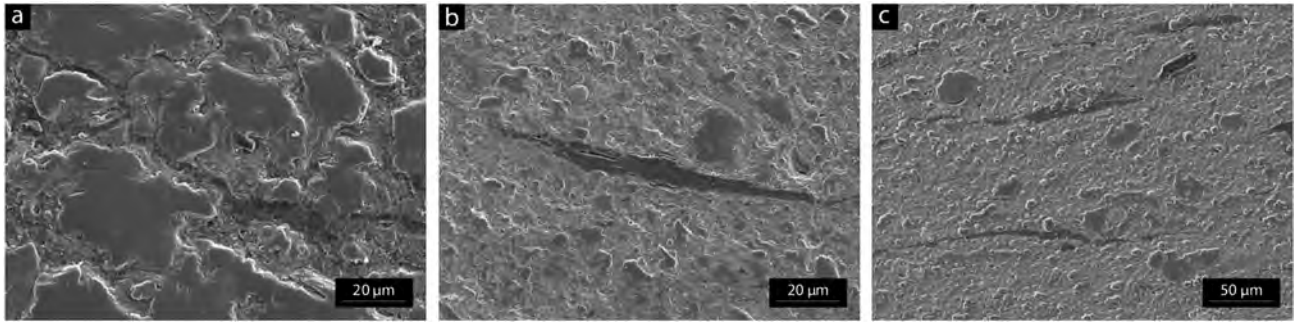[a]R_1 is the Riedel shear angle, plotted in Figure 14.

Figure 15. Secondary electron images of characteristic organic matter microstructures in experimental gouge sample from test series at 30 MPa normal stress; sense of shear is top to the right. (a) Barnett-1, narrow vein of organic matter crossing several clastic contacts at a low angle to the shear plane. (b) Haynesville-1, consolidated lens of organic matter aligned with local clay fabric. (c) Haynesville-2, elongated lenses of organic matter aligned with local clay fabric.

bearing framework, it may play a much more significant role in slip stability and evolution behavior, which may explain the discrepancies in observations of friction rate dependence between this study and Tembe et al. In addition, the coating of clastic contacts at the lowest clay and organic content (e.g., Figure 13d, Barnett-1) may also explain increased prevalence of grain crushing and comminution in the synthetic experiments [*Crawford et al.*, 2008, *Tembe et al.*, 2010] and appears to be evidenced in the mechanical data by relatively greater strain hardening in samples below ~30 wt% clay content. Regardless, the observed transition in friction rate dependence for shale reservoir rocks is generally consistent with established relationships between frictional strength and stability [i.e., *Ikari et al.*, 2011, Figure 11], signifying that although significant differences exist between models of synthetic clay-clastic mixtures and observations of shale gouge friction, we can still apply a grain-packing framework model to explain compositional controls on the frictional properties.

[24] At the lowest clay and organic content, frictional strength is greatest because it is controlled by populations of clastic contacts, which undergo grain-scale fracture and comminution to accommodate slip. No continuous clay fabric is developed at this composition, and clay and organic matter are concentrated in a fine grained matrix coating clastic contacts and filling void space (Figures 13b–13d, Barnett-1). This signifies that the grain-packing framework is composed of clastic particles ~20–100 μm, resulting in the lowest overall contact area and greatest spacing between load-bearing contacts. These micromechanical relationships result in negative friction rate dependence and significant slip-parallel and slip-normal evolution displacements in response to perturbations in slip velocity. The microphysical characteristics of the clastic-supported framework therefore also result in the greatest deviation of the R_1 angle from the bulk shear direction, due to the increase in the gouge framework internal friction [e.g., *Gu and Wong*, 1994].

[25] At moderate clay and organic content, frictional strength decreases as the fraction of clastic contacts decrease and clay aggregates and organic matter further coat these load-bearing contacts, increasing overall contact area within the gouge framework. At this composition, no significant change in the rate of change of layer thickness with shear strain is observed related to initial loading [e.g., *Marone*

and Scholz, 1989], suggesting comminution does not control the onset of shear localization and stable sliding. Additionally, grain-scale fracture and comminution are less prevalent in gouge microstructures and localized lenses of aligned clay aggregates form in the semicontinuous void spaces between clastic contacts (Figure 13f, Eagleford-2), which allow primary shear localization features to rotate toward the bulk shear direction. These microphysical relationships reflect the beginnings of the transition from a clastic-supported to clay and organic matter-supported framework, which manifests in approximately neutral friction rate dependence and decreased slip evolution displacements in response to perturbations in slip velocity.

[26] At the greatest clay and organic content, friction strength is minimized because the load-bearing framework constituted of a continuous clay fabric hosting aligned lenses of organic matter and isolated clasts, which exhibit no evidence of fracture (Figures 13h–13j, Haynesville-3). This signifies that the grain-packing framework is composed of clay aggregate particles ~0.2–1 μm, resulting in the greatest overall contact area and lowest load-bearing contact spacing. Thus, slip is accommodated on clay mineral contacts and clay aggregates contacting organic matter lenses and isolated clasts. The microphysical characteristics of this matrix-supported framework result in strongly positive friction rate dependence and the lowest values of slip evolution displacements in response to perturbations in slip velocity. The formation of a strong clay fabric at this composition allows further rotation of the primary shear localization features to the bulk shear direction, consistent with the degradation of friction strength and the onset of stable sliding.

[27] The correlation of critical slip displacement and dilatancy (Figure 12) as functions of shale composition reflects the micromechanical evolution of the shale grain packing framework described above. *Marone and Kilgore* [1993] observed a similar correlation between critical slip displacement and dilatancy in double-direct shear experiments on quartz sand and found positive correlations of both parameters as a function of increasing grain size, ~1–500 μm. The evolution of the shale grain-packing framework results in a similar variation in grain size of the load-bearing components as clastic contacts are increasingly replaced with clay aggregate contacts with increasing clay and organic content.

However, for shale reservoir rocks, these effects are convolved with changes in grain shape, clay fabric, and resultant contact microstructure, significantly complicating systematic interpretation of gouge microstructure. For example, the slip evolution behavior of samples from each reservoir (Figure 12) shows similar slopes, apparently offset in composition from an overall systematic trend. These variations likely result from the evident microstructural differences in each reservoir as a function of composition (e.g., Figure 2), but may additionally be affected by our simplifying compositional classification that does not account for relative differences in clay and organic matter (e.g., Table 1 and Figure 1). Marone and Kilgore physically interpret the particle size dependence of the slip evolution parameters as a proxy for the region of active shear within the gouge layer, yielding a linear dependence of critical slip displacement on shear band thickness. Although these relationships are evidenced in the shale gouge microstructure through the transition from distributed grain-scale fracture to well-developed shear localization features with increasing clay content, we do not attempt to systematically relate these variations to the observed values of slip evolution parameters in this study.

5.2. Implications for Slip Stability During Reservoir Stimulation

[28] The observed transition from potentially unstable to stable sliding in shale reservoir rocks at a clay and organic content ~30 wt% (Figure 6) has important implications for the expected nature of shear faulting in shale gas reservoirs. As lithologies containing clay and organic content in excess of 30 wt% commonly occur in shale reservoirs [*Ross and Bustin*, 2009; *Passey et al.*, 2010], the frictional stability data suggest that the majority of preexisting faults induced to shear slip would slip stably. If stable shear slip is in fact a ubiquitous phenomenon during hydraulic stimulation of shale reservoirs, it could explain the failure of the shear events associated only with the recorded microseismicity to account for production from these extremely low permeability reservoirs [*Moos et al.*, 2011; *Warpinski et al.*, 2012; Das and Zoback, submitted manuscript, 2013b]. Another potential factor contributing to frequency of slow slip during hydraulic fracturing is that slip on very poorly oriented faults is also expected to be stable independent of composition because the dilatancy and inelastic deformation accompanying shear slip increase the effective normal stress, such that slip is controlled by the diffusion of fluid pressure along the fault [*Zoback et al.*, 2012]. Although slow slip may predominate in these settings, the resultant dilatancy and inelastic deformation still appear to contribute significantly to permeability during hydraulic stimulation. In fact, I. Das and M. D. Zoback (submitted manuscript, 2013a) calculate that the cumulative moment release from LPLD events represents ~10% of the total fluid injection energy for the corresponding hydraulic fracturing operations whereas the cumulative moment release from microearthquakes only accounts for ~0.1%.

[29] *Vermylen and Zoback* [2011] describe a series of hydraulic fracturing experiments performed in the Barnett shale, Texas, nearby which Das and Zoback (submitted manuscript, 2013a) found LPLD events interpreted to originate from slowly slipping faults in the reservoir. The Barnett samples studied here were cored from a nearby well in the same reservoir. In these operations, typical of many multistage hydraulic

fracturing operations in shale gas reservoirs, ~1500 m long horizontal wells were fractured in ~100 m stages, sequentially isolated and pressurized. Microseismic monitoring of each stage was performed using borehole arrays of 15 Hz geophones placed in adjacent vertical or horizontal wells. A number of the LPLD events were coincident with several microearthquakes on a plane striking parallel to the dominant natural fracture direction obtained from borehole image logs. *Das and Zoback* [2011] interpret this plane to be a relatively large, slowly slipping preexisting fault, the source of both the LPLD events and the microearthquakes. Similar low-frequency events have been observed in microseismic data sets from other shale gas reservoirs (Das and Zoback, submitted manuscript, 2013a, 2013b), motivating further investigation of the microphysical processes controlling the transition from seismic to subseismic responses in shale reservoir rocks.

5.3. Microseismic Event Magnitudes and Slow Slip

[30] We consider the observations of rate-state constitutive parameters in context of the critical fault patch size required for initiating slip on preexisting faults and associated microearthquake magnitudes. Classic studies of spring-slider systems governed by rate-state friction [*Dieterich*, 1979; *Ruina*, 1983] establish that for instability to occur, the system stiffness k, must be less than a critical value k_c, given by

$$k_c = \frac{(b-a)\sigma_n}{d_c} \quad (7)$$

Dieterich [1992] represents conditions for slip instability on a fault as a crack embedded in an elastic medium, with approximate effective stiffness:

$$k = \frac{\Delta\tau}{\delta} = \frac{G}{l} \quad (8)$$

in which $\Delta\tau$ is the stress drop and δ is the slip in the solution for displacement along the crack. G is the shear modulus and l is the crack or fault patch length. Combining these relations yields the minimum patch dimension for unstable fault slip, l_c:

$$l_c = \frac{Gd_c}{(b-a)\sigma_n} \quad (9)$$

[31] Fault patches with dimensions less than l_c will have $k > k_c$ and will always slip stably, while those above the critical dimension may slip unstably. Thus, we are able to utilize the measurements of d_c and $(a-b)$ reported here, those of G derived from the elastic parameters for shale samples from the same wells (Sone and Zoback, submitted manuscript, 2013a), and the relevant stress magnitudes, $S_v = 75$ MPa, $S_{h\max} = 60$ MPa, and $S_{h\min} = 45$ MPa [*Vermylen*, 2011], to examine the relationship between l_c and fault size under different conditions of hydraulic stimulation. The estimates of stress magnitudes and stimulation pore pressures combined with the constraints on frictional strength in shale reservoirs developed in this study enable direct estimates of the effective normal stress during slip. When slip occurs on well-oriented faults in response to small perturbations in pore pressure, $\sigma_n \sim 10$–20 MPa. However, slip only occurs on poorly oriented faults when pore pressure is extremely high due to active pumping during hydraulic stimulation, resulting in $\sigma_n \sim 1$–5 MPa. Taking

G = 20 GPa, d_c = 25–50 μm, and $(b − a)$ = 0.005–0.0025, based on the most strongly rate-weakening samples in our study, we find l_c = 5–40 m for relatively well-oriented faults and l_c = 20–400 m for poorly oriented faults.

[32] Microearthquake magnitudes are typically −1 to −3 during hydraulic fracturing [*Shemeta and Anderson*, 2010; *Warpinski et al.*, 2012], so assuming a Brune circular crack model [*Brune*, 1970] and typical stress drop ~0.1–10 MPa [*Kwiatek et al.*, 2011], these events imply fault patch sizes ~0.5–8 m, generally consistent with the laboratory-derived constraints on the critical patch size for microearthquakes induced on well-oriented faults in shale reservoirs. In contrast, the critical patch size for slip on poorly oriented faults is much greater than the implied fault size associated with the magnitude of typical microseismic events, signifying that slip on large, poorly oriented faults at low effective normal stress is expected to be stable or subseismic. These characteristics are consistent with the hypothesized model of *Das and Zoback* [2011, also submitted manuscript, 2013b], which attributes observed LPLD events to slow slip on large preexisting reservoir faults.

[33] While this analysis provides important insights into the mechanisms of induced slip during hydraulic stimulation, several simplifying assumptions need to be addressed in future investigations of shale reservoir deformation. First, we attempt to relate the results of the dry, room temperature friction experiments to the in situ behavior of faults in shale reservoirs. Although the samples in this study are sourced from shale facies saturated with dry gas, during hydraulic stimulation, there are essentially no established constraints on the in situ pore fluid accompanying induced slip. Therefore, it is difficult to motivate the use of different potential pore fluid phases in the experiments while simultaneously examining the compositional controls on frictional and micromechanical properties. Future studies focusing on the systematic effects of in situ pore fluid over the range of shale composition are necessary to establish further constraints on the deformation mechanisms during induced slip. Additionally, in both the friction experiments and the critical patch size analysis, we assert a constant normal stress condition on the fault plane. During hydraulic stimulation, the hydrologic loading path, i.e., the change in effective normal stress due to active pumping may vary significantly in time and between faults of different lithologies and orientations. Therefore, it is conceivable that there exists a loading-rate dependence of frictional stability, which represents another potential mechanism for dissipation of the fluid injection energy during stimulation; however, we are again not able to comment on this directly due to the constant normal stress boundary conditions of the experiments. Further studies of slip stability in this context are needed and may provide more general insights into the connections between lithology, fault orientation, and hydrologic properties for injection-induced earthquakes.

6. Conclusions

[34] We performed laboratory experiments on natural shale samples from three hydrocarbon reservoirs to systematically investigate the effects of clay and organic content on the frictional behavior of shale reservoir rocks. We observed decreasing frictional strength with increasing clay and organic content, as well as a transition in frictional rate dependence from velocity weakening to velocity strengthening at ~30 wt%.

We additionally examined slip evolution behavior as a function of shale composition and found negative correlations of independently measured slip-parallel and slip-normal evolution displacements with increasing clay and organic content. These mechanical data are supplemented by microstructural observations of the experimental shale gouges, which physically illustrate the evolution of the shale grain packing framework as a function of composition through macroscopic expressions of shear localization and microphysical contact-scale relationships. We utilize these lines of evidence to inform a micromechanical model of the effects of clay and organic content on the frictional properties of shale reservoir rocks.

[35] When considering the laboratory friction data in the context of observed microseismicity during multistage hydraulic fracturing, there would appear to be appreciable slow slip also occurring on preexisting faults, as these reservoirs are commonly constituted of lithologies with >30 wt% clay and organic content. The frictional stability data presented here suggest that stable slip on preexisting faults may be a ubiquitous phenomenon during hydraulic stimulation of shale reservoirs, which addresses the observed discrepancies between production, permeability enhancement, and cumulative microseismic deformation. Utilizing the experimentally determined friction constitutive parameters and estimates of the variation in effective normal stress for induced slip, we constrain the likely magnitudes of the microseismic events by examining the critical fault patch size required for instability on well-oriented faults, which is consistent with the implied source dimensions of recorded event magnitudes. Additionally, we demonstrate that for the case of poorly oriented faults, the implied source dimensions cannot be explained by the estimated critical fault patch size, signifying that slip on large, preexisting reservoir faults during hydraulic fracturing is expected to be stable.

[36] The results of this study begin to inform our understanding of the spectrum of deformation mechanisms active during induced fault slip in shale reservoirs. The emergence of hydraulic fracturing operations in these settings represents a significant opportunity to investigate microseismicity and slow slip, which can contribute directly to our understanding of analogous processes in tectonic settings. Further investigation of the relationships between stimulation, deformation mechanisms, and production are therefore warranted, particularly as hydraulic fracturing develops into a widespread energy production strategy.

Notation

f Coefficient of sliding friction
$(a − b)$ Rate-state frictional stability parameter
Δf_{ss} Change in steady state friction in response to a step change in slip velocity
V Slip velocity (μm s^{-1})
V_0 Reference slip velocity (μm s^{-1})
θ State variable (s)
a Rate-state direct effect parameter
b Rate-state evolution effect parameter
d_c Critical slip displacement (μm)
K Normalized apparatus stiffness (mm^{-1})
V_{lp} Load point velocity (μm s^{-1})
α Dilatancy parameter

Δh Change in layer thickness in response to a step change in slip velocity (μm)

h Gouge layer thickness (mm)

τ Applied shear stress on sawcut (MPa)

σ_n Applied effective normal stress on sawcut (MPa)

σ_a Applied axial stress (MPa)

P Applied confining pressure (MPa)

Ψ Angle between core axis and saw-cut plane (deg)

R_1 Primary Riedel shear angle (deg)

k_c Rate-state critical stiffness (MPa m^{-1})

k Critical stiffness of a circular crack (MPa m^{-1})

$\Delta\tau$ Crack stress drop (MPa)

δ Crack slip displacement (mm)

G Elastic shear modulus (GPa)

l Fault patch or crack length (m)

l_c Minimum patch size required for instability (m)

S_v Vertical principal stress (MPa)

$S_{h\max}$ Maximum horizontal principal stress (MPa)

$S_{h\min}$ Minimum horizontal principal stress (MPa)

References

Ahmadov, R. (2011), Microtextural, elastic and transport properties of source rocks, *Stanford Rock Physics and Borehole Geophysics Thesis*, *127*, Stanford University, Stanford, CA.

Beroza, G. C., and S. Ide (2009), Deep tremors and slow quakes, *Science*, *324*, 1025–1026, doi:10.1126/science.1171231.

Bird, P. (1984), Hydration-phase diagrams and friction of montmorillonite under laboratory and geologic conditions, with implications for shale compaction, slope stability, and strength of fault gouge, *Tectonophysics*, *107*, 235–260.

Blanpied, M. L., C. J. Marone, D. A. Lockner, J. D. Byerlee, and D. P. King (1998), Quantitative measure of the variation in fault rheology due to fluid-rock interactions, *J. Geophys. Res.*, *103*(98), 9691–9712.

Brune, J. N. (1970), Tectonic stress and the spectra of seismic shear waves from earthquakes, *J. Geophys. Res.*, *75*(26), 4997–5009.

Byerlee, J. D. (1978), Friction of rocks, *Pure Appl. Geophys.*, *116*, 615–626.

Cathles, L. M. (2012), Assessing the greenhouse impact of natural gas, *Geochem. Geophys. Geosyst.*, *13*, Q06013, doi:10.1029/2012GC004032.

Chester, F. M., J. P. Evans, and R. L. Biegel (1987), Internal structure and weakening mechanisms of the San Andreas Fault, *J. Geophys. Res.*, *98*(B1), 771–786.

Chester, F. M., J. J. Mori, S. Toczko, and N. Eguchi (2012), Expedition 343/343T preliminary report Japan Trench Fast Drilling Project (JFAST), *IODP Prel. Rept.*, 343/343T, doi:10.2204/iodp.pr.343343T.2012.

Crawford, B. R., D. R. Faulkner, and E. H. Rutter (2008), Strength, porosity, and permeability development during hydrostatic and shear loading of synthetic quartz-clay fault gouge, *J. Geophys. Res.*, *113*, B03207, doi:10.1029/2006JB004634.

Curtis, C. D. (1980), Diagenetic alteration in black shales, *J. Geol. Soc.*, *137*, 189–194.

Das, I., and M. D. Zoback (2011), Long-period, long-duration seismic events during hydraulic fracturing stimulation of a shale gas reservoir, *Leading Edge*, July 2011, *30*, 778–787, doi:10.1190/1.3609093.

Deng, X., and M. B. Underwood (2001), Abundance of smectite and the location of a plate-boundary fault, Barbados accretionary prism, *Geol. Soc. Am. Bull.*, *113*(4), 495–507.

den Hartog, S. A. M., C. J. Peach, D. A. M. de Winter, C. J. Spiers, and T. Shimamoto (2012), Frictional properties of megathrust fault gouges at low sliding velocities: New data on the effects of normal stress and temperature, *J. Struct. Geol.*, *38*, 156–171, doi:10.1016/j.jsg.2011.12.001.

Dieterich, J. H. (1979), Modeling of rock friction 1. Experimental results and constitutive equations, *J. Geophys. Res.*, *84*(B5), 2161–2168.

Dieterich, J. H. (1992), Earthquake nucleation on faults with rate-and state-dependent strength, *Tectonophysics*, *211*, 115–134.

Dieterich, J. H., and B. D. Kilgore (1994), Direct observation of frictional contacts: New insights for state-dependent properties, *Pure Appl. Geophys.*, *143*, 283–302.

Flavin, C., and S. Kitasei (2010), The role of natural gas in a low-carbon energy economy, *WorldWatch Institute*, April 2010.

Gu, Y., and T.-F. Wong (1994), Development of shear localization in simulated quartz gouge: Effect of cumulative slip and gouge particle size, *Pure Appl. Geophys.*, *143*, 387–424.

Ikari, M. J. (2010), Compositional, mechanical and hydrologic controls on fault slip behavior, *Pennsylvania State University Thesis*, August 2010, The Pennsylvania State University, University Park, PA.

Ikari, M. J., D. M. Saffer, and C. Marone (2007), Effect of hydration state on the frictional properties of montmorillonite-based fault gouge, *J. Geophys. Res.*, *112*, B06423, doi:10.1029/2006JB004748.

Ikari, M. J., D. M. Saffer, and C. Marone (2009), Frictional and hydrologic properties of clay-rich fault gouge, *J. Geophys. Res.*, *114*, B05409, doi:10.1029/2008JB006089.

Ikari, M. J., C. Marone, and D. M. Saffer (2011), On the relation between fault strength and frictional stability, *Geology*, *39*(1), 83–86, doi:10.1130/G31416.1.

Kwiatek, G., K. Plenkers, and G. Dresen (2011), Source parameters of picoseismicity recorded at Mponeng Deep Gold Mine, South Africa: Implications for scaling relations, *Bull. Seismol. Soc. Am.*, *101*(6), 2592–2608, doi:10.1785/0120110094.

Liu, Y., and A. M. Rubin (2010), Role of fault gouge dilatancy on aseismic deformation transients, *J. Geophys. Res.*, *115*, B10414, doi:10.1029/2010JB007522.

Logan, J. M., C. A. Dengo, N. G. Higgs, and Z. Z. Wang (1992), Fabrics of experimental fault zones: Their development and relationship to mechanical behavior, in *Fault Mechanics and Transport Properties of Rocks*, edited by B. Evans and T.-F. Wong, pp. 33–67, Academic Press, New York.

Lupini, J. F., A. E. Skinner, and P. R. Vaughan (1981), The drained residual strength of cohesive soils, *Geotechnique*, *31*, 181–213.

Mandl, G., and R. F. Luque (1977), Fully developed plastic shear flow of granular materials, *Geotechnique*, *20*, 277–307.

Mandl, G., L. N. J. de Jong, and A. Maltha (1977), Shear zones in granular material: An experimental study of their structure and mechanical genesis, *Rock Mech.*, *9*, 95–144, doi:10.1007/BF01237876.

Marone, C. (1998), Laboratory-derived friction laws and their application to seismic faulting, *Annu. Rev. Earth Planet. Sci.*, *26*(1), 643–696.

Marone, C., and B. Kilgore (1993), Scaling of the critical slip distance for seismic faulting with shear strain in fault zones, *Nature*, *362*, 618–620.

Marone, C., and C. H. Scholz (1989), Particle-size distribution and microstructures within simulated fault gouge, *J. Struct. Geol.*, *11*(7), 799–814.

Marone, C., C. B. Raleigh, and C. H. Scholz (1990), Frictional behavior and constitutive modeling of simulated fault gouge, *J. Geophys. Res.*, *95*(B5), 7007–7025.

Moon, C. F. (1972), The microstructure of clay sediments, *Earth Sci. Rev.*, *8*(3), 303–321.

Moore, D. E., and D. A. Lockner (2007), Friction of the smectite clay montmorillonite, in *The Seismogenic Zone of Subduction Thrust Faults*, edited by T. Dixon and C. Moore, pp. 317–345, Columbia University Press, New York.

Moore, D. E., and D. A. Lockner (2011), Frictional strengths of talc-serpentine and talc-quartz mixtures, *J. Geophys. Res.*, *116*, B10414, doi:10.1029/2010JB007522.

Moos, D., G. Vassilellis, R. Cade, J. Franquet, B. Hughes, A. Lacazette, P. Company, E. Bourtembourg, G. Daniel, and M. Sas (2011), Predicting shale reservoir response to stimulation in the Upper Devonian of West Virginia, *Soc. Pet. Eng.*, 145849 November 2011, doi:10.2118/145849-MS.

Obara, K. (2002), Nonvolcanic deep tremor associated with subduction in southwest Japan, *Science*, *296*, 1679–1681, doi:10.1126/science.1070378.

Passey, Q. R., K. M. Bohacs, W. L. Esch, R. Klimentidis, and S. Sinha (2010), From oil-prone source rock to gas-producing shale reservoir—Geologic and petrophysical characterization of unconventional shale-gas reservoirs, *Soc. Pet. Eng.*, 131350, June 2010, doi:10.2118/131350-MS.

Peng, Z., and J. Gomberg (2010), An integrated perspective of the continuum between earthquakes and slow-slip phenomena, *Nat. Geosci.*, *3*, 599–607, doi:10.1038/ngeo940.

Reinen, L. A., and J. D. Weeks (1993), Determination of rock friction constitutive parameters using an iterative least squares inversion method, *J. Geophys. Res.*, *98*(B9), 15,937–15,950.

Revil, A., D. Grauls, and O. Brevart (2002), Mechanical compaction of sand/clay mixtures, *J. Geophys. Res.*, *107*(B11), 2293, doi:10.1029/2001JB000318.

Ross, D. J. K., and R. Marc Bustin (2009), The importance of shale composition and pore structure upon gas storage potential of shale gas reservoirs, *Mar. Pet. Geol.*, *26*, 916–927, doi:10.1016/j.marpetgeo.2008.06.004.

Ruina, A. L. (1983), Slip instability and state variable friction laws, *J. Geophys. Res.*, *88*(B12), 10,359–10,370.

Saffer, D. M., and C. Marone (2003), Comparison of smectite- and illite-rich gouge frictional properties: Application to the updip limit of the seismogenic zone along subduction megathrusts, *Earth Planet. Sci. Lett.*, *215*, 219–235, doi:10.1016/S0012-821X(03)00424-2.

Saffer, D. M., M. Frye, C. Marone, and K. Mair (2001), Laboratory results indicating complex and potentially unstable frictional behavior of smectite clay, *Geophys. Res. Lett.*, *28*(12), 2297–2300.

Samuelson, J., D. Elsworth, and C. Marone (2009), Shear-induced dilatancy of fluid-saturated faults: Experiment and theory, *J. Geophys. Res.*, *114*, B12404, doi:10.1029/2008JB006273.

Schleicher, A. M., B. A. van der Pluijm, and L. N. Warr (2010), Nanocoatings of clay and creep of the San Andreas fault at Parkfield California, *Geology*, *38*, 667–670, doi:10.1130/G31091.

Scott, D. R., C. J. Marone, and C. G. Sammis (1994), The apparent friction of granular fault gouge in sheared layers, *J. Geophys. Res.*, *99*(B4), 7231–7246.

Segall, P., and J. R. Rice (1995), Dilatancy, compaction, and slip instability of a fluid-infiltrated fault, *J. Geophys. Res.*, *100*(B11), 22,155–22,171.

Segall, P., A. M. Rubin, A. M. Bradley, and J. R. Rice (2010), Dilatant strengthening as a mechanism for slow slip events, *J. Geophys. Res.*, *115*, B12305, doi:10.1029/2010JB007449.

Shelly, D. R., G. C. Beroza, and S. Ide (2007), Non-volcanic tremor and low-frequency earthquake swarms, *Nature*, *446*, 305–307, doi:10.1038/nature05666.

Shemeta, J., and P. Anderson (2010), It's a matter of size: Magnitude and moment estimates for microseismic data, *Leading Edge*, March 2010, *29*, 296–302, doi:10.1190/1.3353726.

Shimamoto, T., and J. M. Logan (1981), Effects of simulated clay gouges on the sliding behavior of Tennessee sandstone, *Tectonophysics*, *75*, 243–255.

Skempton, A. W. (1964), Long-term stability of clay slopes, *Geotechnique*, *14*, 77–102.

Solum, J. G., S. H. Hickman, D. A. Lockner, D. E. Moore, B. A. van der Pluijm, A. M. Schleicher, and J. P. Evans (2006), Mineralogical characterization of protolith and fault rocks from the SAFOD Main Hole, *Geophys. Res. Lett.*, *33*, L21314, doi:10.1029/2006GL027285.

Summers, R., and J. D. Byerlee (1977), A note on the effect of fault gouge composition on the stability of frictional sliding, *Int. J. Rock Mech. Min. Sci.*, *14*, 155–160.

Takahashi, M., K. Mizoguchi, K. Kitamura, and K. Masuda (2007), Effects of clay content on the frictional strength and fluid transport property of faults, *J. Geophys. Res.*, *112*, B08206, doi:10.1029/2006JB004678.

Tembe, S., D. A. Lockner, and T.-F. Wong (2010), Effect of clay content and mineralogy on frictional sliding behavior of simulated gouges: Binary and ternary mixtures of quartz, illite, and montmorillonite, *J. Geophys. Res.*, *115*, B03416, doi:10.1029/2009JB006383.

Underwood, M. B. (2002), Strike-parallel variations in clay minerals and fault vergence in the Cascadia subduction zone, *Geology*, *30*, 155–158, doi:10.1130/0091-7613.

Vermylen, J. P. (2011), Geomechanical studies of the Barnett shale, Texas, USA, *Stanford Rock Physics and Borehole Geophysics Thesis*, *125*, Stanford University, Stanford, CA.

Vermylen, J. P., and M. D. Zoback (2011), Hydraulic Fracturing, Microseismic magnitudes, and stress evolution in the Barnett shale, Texas, USA, *Soc. Pet. Eng.*, 140507, January 2011, doi:10.2118/140507-MS.

Vrolijk, P. (1990), On the mechanical role of smectite in subduction zones, *Geology*, *18*, 703–707.

Vrolijk, P., and B. A. van der Pluijm (1999), Clay gouge, *J. Struct. Geol.*, *21*, 1039–1048.

Warpinski, N. R., J. Du, U. Zimmer, and P.-A. H. Service (2012), Measurements of hydraulic-fracture-induced seismicity in gas shales, *Soc. Pet. Eng.*, 151597, February 2012, doi:10.2118/151597-MS.

Zoback, M. D. (2007), *Reservoir Geomechanics*, pp. 459, Cambridge Univ. Press, New York.

Zoback, M. D., S. Kitasei, and B. Copithorne (2010), Addressing the environmental risks from shale gas development, *WorldWatch Institute*, July 2010.

Zoback, M. D., A. H. Kohli, I. Das, and M. McClure (2012), The importance of slow slip on faults during hydraulic fracturing stimulation of shale gas reservoirs, *Soc. Pet. Eng.*, 155476, June 2012, doi:10.2118/155476-MS.